

Design and fabrication of button-style beam position monitors for the HEPS synchrotron light facility

Jun He^{1*}, Yan-Feng Sui^{1,2}, Yong Li^{1,2}, Xu-Hui Tang^{1,2}, Lin Wang¹, Fang Liu¹, Zhi Liu¹, Ling-Da Yu¹, Xiao-Yu Liu¹, Tao-Guang Xu¹, Jian-She Cao (<https://orcid.org/0000-0001-6507-2636>)^{1,2}, Jun-Hui Yue^{1**}

¹ Key Laboratory of Particle Acceleration Physics and Technology, Institute of High Energy Physics, Chinese Academy of Sciences, Beijing 100049, China
² University of Chinese Academy of Sciences, Beijing 100049, China.

Corresponding author, [*hejun@ihep.ac.cn](mailto:hejun@ihep.ac.cn); [**yuejh@ihep.ac.cn](mailto:yuejh@ihep.ac.cn)

This work was supported by the Youth Innovation Promotion Association CAS (Nos. 2019013 and Y202005) and the National Natural Science Foundation of China (No. 11975254).

Abstract

At the High Energy Photon Source (HEPS), a high orbital stability of typically 10 % of the beam size and angular divergence must be achieved. The beam size at the insertion devices is 10 μm horizontally and 1 μm vertically, which implies that the beam orbit must be stabilized to the sub-micrometer level. This results in stringent tolerance and quality control requirements for the series production of beam position monitor (BPM) pickups. In this study, analytical formulas were used and CST simulations were performed to analyze the effects of the mechanical tolerances of BPM pickups on beam position measurement. The results of electromagnetic field simulations revealed how various mechanical errors, such as button size and location accuracy, as well as the related button capacitance, exert different influences on the beam position measurement. The performance of an actual BPM pickup was measured, along with an assessment of the error on the beam position measurement. Additionally, a wakefield analysis, including an investigation of trapped resonant modes and related thermal deformation, was conducted.

Keywords High Energy Photon Source · BPM · Error · CST · Tolerances

1. Introduction

The High Energy Photon Source (HEPS) is the first fourth-generation light source currently under construction in Beijing, China [1, 2]. It is designed with a natural emittance of 34 pmrad and a brightness of 10^{22} photons s^{-1} mm^{-2} mrad^{-2} (0.1% Bandwidth) $^{-1}$ to provide high-performance X-rays with energies up to 300 keV for various basic scientific investigations [3, 4]. To achieve sub-micrometer orbit stability, accurate beam position measurements and orbit feedback systems are crucial. The beam position monitor (BPM) pickup and related read-out electronics determine the precision of beam position measurement. The beam signals induced by image charges on button-style BPM electrodes are transferred from inside the vacuum pipe to outside via a coaxial vacuum feedthrough. Typically, the button BPM electrodes and ultra-high vacuum Radio Frequency (RF) feedthrough are combined in a single component, as shown in Fig. 1.

To achieve the required beam orbit measurement resolution of 0.1 μm , we are currently investigating BPM pickups and related read-out electronics [5–7]. To meet orbit stabilization requirements, fast orbit feedback systems [8–11] and a high stability support structure [12–15] have been studied. The HEPS comprises five types (A–E) of button-style BPMs, and their cross-sections are shown in Fig. 1. The numbers in the figure represent the mechanical dimensions in millimeters. Types A, B, and C are located in the storage ring, whereas Types D and E are located in the booster. Approximately 600 BPMs will be installed, and all BPMs will utilize the same button feedthrough, the main mechanical parameters of which are shown in Fig. 1f. The HEPS storage ring contains 48 seven-bend achromat (7BA) cells [1], each equipped with 12 BPMs, where the 1st–7th and 10th–12th BPMs are Type A and the 8th and 9th BPMs are Types B and C, respectively.

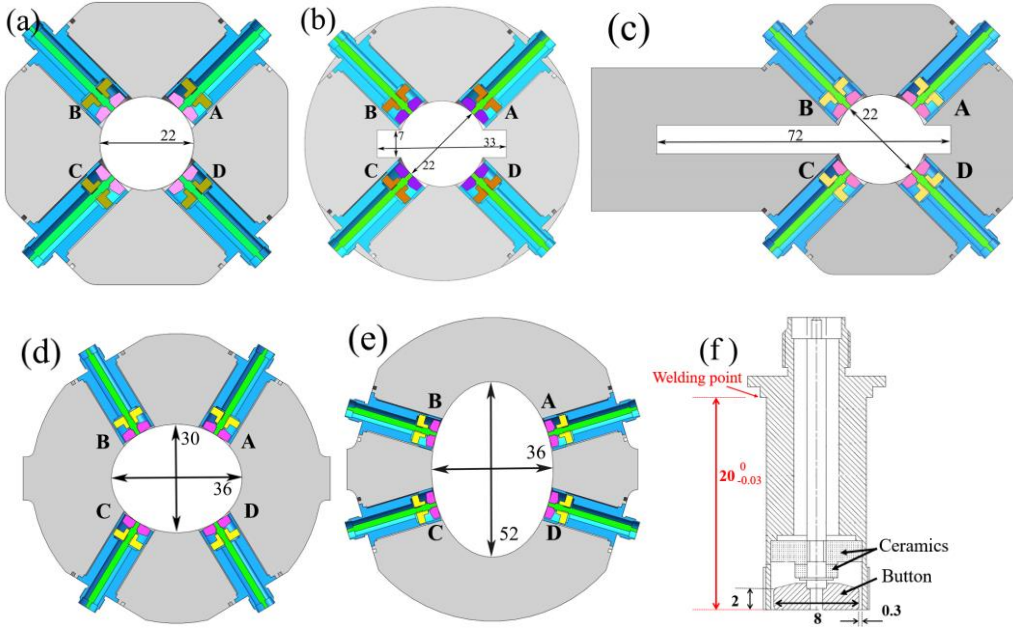


Fig. 1 (Color online) Five button-style BPMs (a–e) and the feedthrough for the HEPS (f).

In this study, the effects of the mechanical tolerances of BPM pickups on beam position measurement were investigated to aid designers with a reasonable tolerance based on the error budget. Typically, mechanical tolerances are closely related to production costs and should be determined based on the criticality of an item. The measurement of the mechanical tolerances of a BPM button electrode, characterization of the button-to-ground capacitance, and analysis of the deformation of the feedthrough after the welding procedure are essential for its use as a BPM; however, this investigation requires a significant amount of effort. Sorting the feedthroughs based on measurement data can improve the required mechanical and electrical symmetry, thus reducing the tolerances. A good balance between costs and requirements can only be determined based on the measurement results. Herein, we list statistical data from the fabricated BPM process performed for the HEPS, such as the BPM button radius, button capacitance, and the precision of its location, that is, the positioning of the button feedthrough in the BPM housing. We referred to previous studies to develop the feedthroughs [16–19]. Furthermore, the trapped resonant modes of the BPM caused by wakefields and their effects on temperature and thermal deformation are discussed.

2. Analytical estimation of the transfer impedance of the HEPS button BPM

The BPM transfer impedance $Z_t(\omega)$ describes the BPM voltage response signal $V(\omega)$ to the bunched beam current signal $I(\omega)$, as given by Ohm's law:

$$V(\omega) = Z_t(\omega) \times I(\omega), \quad (1)$$

$Z_t(\omega)$ is an important characteristic of a BPM pickup and is defined by the shape and dimensions of BPM geometry [20–22]. It is a function of angular frequency ω and has a high-pass filter-like frequency characteristic. For broadband BPM pickups, such as button-style electrodes, the beam-position behavior is frequency-independent. In practice, Z_t is typically of the order of $\sim 1 \Omega$ at frequencies > 1 GHz, which indirectly defines the resolution potential of a button BPM connected to adequate read-out electronics. There are three methods of determining Z_t . First, in the equivalent

circuit method [21,22], the beam current signal is represented as a current source and the BPM button electrode is represented as the capacitance C_b in parallel to the load resistor R_0 . Second, electromagnetic (EM) field analysis with the bunched beam as a line charge stimulus signal can be used to calculate the response of the BPM to the beam [23]. Third, an experimental method can be used, in which an antenna in a BPM calibration system is used to simulate the beam, and the response of the BPM can be inferred from the analysis of an S-parameter measurement [24].

Researchers at DAFNE have derived analytical expressions for the transfer impedance Z_t , longitudinal beam-coupling impedance Z_l , and signal power $\langle P \rangle$ output from a button BPM electrode, which can be used to determine basic parameters in the early stages of development [25].

$$Z_t = \frac{r_b^2 R_0 \omega}{2bc(1+R_0^2 C_b^2 \omega^2)} (R_0 C_b \omega + j), \quad (2)$$

$$Z_l = \frac{r_b^4 \omega}{4b^2 c^2 C_b (1+R_0^2 C_b^2 \omega^2)} (R_0 C_b \omega + j), \quad (3)$$

$$\langle P \rangle = \frac{I^2 r_b^4 \omega^2 R_0}{8b^2 c^2 (1+R_0^2 C_b^2 \omega^2)}, \quad (4)$$

where r_b is the button radius, C_b is the button capacitance to the ground, b is the distance between the beam and BPM button (that is, the beam pipe radius for a circular beam pipe with the beam in the center), R_0 is the load impedance of the BPM electronics (50 Ω in the HEPS), c is the speed of light, and I is the beam current. These equations hold only for relativistic beams with $\beta \approx 1$, where all EM field components of the charged particles are purely transverse (TEM field). At lower beam velocities, $\beta \ll 1$, the EM field of a charged particle develops longitudinal field components, in which the BPM response also depends on β [22].

The transfer impedances of five different button-style BPMs were calculated using CST and are shown in Fig. 2a (lower graph), along with the spectrum of a Gaussian beam bunch with an root mean square (RMS) length of 10 mm, indicated by a red dashed trace. This leads to the output signal $V(\omega)$ via multiplication of the bunch spectrum with transfer impedance. As illustrated in Fig. 2a, the transfer impedances of the Type-B and C BPMs were similar and slightly higher than that of Type A, which is related to the horizontal slot used to guide the synchrotron radiation. Note that the differences between Type B(C) and Type A are minor and will be ignored in the following; they will both hereafter be referred to as Type A. The main mechanical parameters of the feedthrough are shown in Fig. 1f. Figures 2b and c illustrate the impact of different button capacitances C_b and button radii r_b on the transfer impedance, Fig. 2b with $C_b = 1-5$ pF ($r_b = 4$ mm is fixed), and Fig. 2c with $r_b = 1-5$ mm ($C_b = 3$ pF is fixed). As given by Eq. (2), increasing the button diameter and decreasing the button capacitance result in a higher transfer impedance. Although these parameters can be changed independently in Eq. (2), in practice, C_b depends on r_b . The capacitance of the feedthrough can be approximated as the sum of the capacitances of the individual components [26].

$$C_{\text{feedthrough}} = C_{\text{button}} + C_{\text{dielectric}} + C_{\text{pin}} + C_{\text{fringe}}. \quad (5)$$

The capacitance C_{coax} of a short piece of coaxial transmission line of length l_{coax} can be calculated analytically by neglecting the fringe field effects [27].

$$C_{\text{coax}} = \frac{2\pi\epsilon l_{\text{coax}}}{\ln\left(\frac{R_{\text{out}}}{R_{\text{in}}}\right)}, \quad (6)$$

where R_{out} is the inner radius of the outer conductor, R_{in} is the outer radius of the inner conductor, ϵ is the dielectric constant of the material between the outer and inner conductors, and l_{coax} is the coaxial structural length. The numerical CST simulation involves an EM-field analysis, which intrinsically includes all dependencies, and therefore provides more accurate results, as shown in Fig. 2a, compared to the analytical approximation shown in Fig. 2b (and c). The transfer impedance at the read-out electronics processing frequency is mainly determined by the button radius, not by the capacitance. In practice, we can always treat the different button feedthrough dimensions with the same capacitance of 2.5 pF, and the error on the transfer impedance remained within 10 % for our choice of feedthrough dimensions.

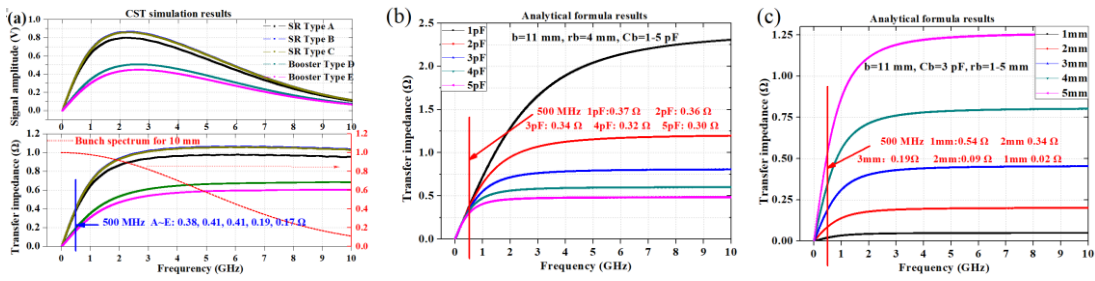


Fig. 2 (Color online) (a) Transfer impedance of five types of HEPS button BPMs calculated using the CST Wakefield solver. Transfer impedance for different (b) capacitances and (c) button radii, calculated using Eq. (2) with the Type-A BPM.

Many different methods can be used to process BPM signals in read-out electronics [28–30]. Frequency-selective BPM signal processing is the most popular method used for electron storage rings. The transfer impedances Z_t at two very different frequencies, 200 MHz and 5 GHz, are shown in Figs. 3a and b as functions of the button radius r_b and capacitance C_b . The low-frequency case in Fig. 3a exhibited a transfer impedance that was almost independent of the button capacitance C_b , whereas it varied for the high-frequency case (Fig. 3b). The signal processing frequency of the in-house developed HEPS read-out electronics was chosen to be 500 MHz. Fig. 3c illustrates the corresponding signal power calculated using Eq. (4) for $C_b = 2.2\text{--}2.4$ pF and $r_b = (3.8\text{--}4.2)$ mm. For a beam current of 200 mA, the expected signal power was approximately -13 ± 1 dBm. At an operating frequency of 500 MHz, the analytically calculated transfer impedance of the three BPM types A, D, and E were 0.38, 0.26, and 0.21 Ω compared with 0.38, 0.19, and 0.17 Ω from the numerical CST analysis, respectively. Eqs. (2–4) are only valid for a circular pipe, which differs when compared with CST simulation for Types D and E. Table 1 lists the transfer impedances and signal powers of other synchrotron light sources and electron storage ring button BPM pickups, calculated using Eqs. (2) and (4), at a frequency of 500 MHz. When a reference capacitance could not be obtained from literature, a value of 2.5 pF was used.

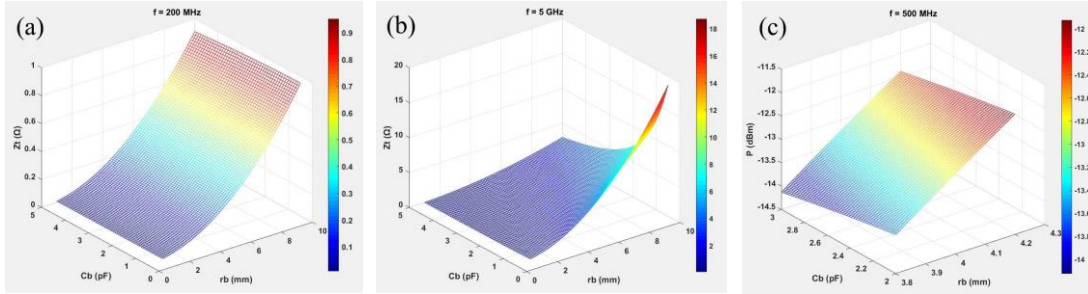


Fig. 3 (Color online) Transfer impedance and signal power with different r_b and C_b . **(a)** $f = 200$ MHz. **(b)** $f = 5$ GHz. **(c)** Signal power with different r_b and C_b ; $f = 500$ MHz and $I = 200$ mA.

Table 1 Transfer impedance and signal power ($I = 200$ mA) of other light sources and colliders, calculated using Eqs. (2) and (4), at an operating frequency of 500 MHz

Lab	Button radius, r_b (mm)	Half aperture, b (mm)	Button capacitance, C_b (pF)	Transfer impedance, Z_t (Ω)	Power (dBm)	Ref.
SPring8	9	15	2.5*	1.414	-1.6	[31]
APS-U	5	11	2.6	0.595	-9.2	[26]
ESRF	5.5	15	2.5*	0.528	-10.2	[31]
BEPCII	7.5	30	2.2	0.491	-10.7	[32]
SSRF-Arc	5	15.3	2.4	0.428	-11.9	[27, 33]
DIMOND	5.4	18.5	2.5*	0.413	-12.3	[34]
HEPS-A	4	11	2.4	0.381	-12.9	
SSRF-HD	5	18.8	2.4	0.348	-13.7	[27, 33]
APS	5	19	2.6	0.344	-13.9	[31]
SPring8-II	3.5	10	2.5*	0.321	-14.5	[35]
ESRF-EBS1	4	13.3	2.5*	0.315	-14.6	[19]
ESRF-EBS2	3	7.9	2.5*	0.298	-15.1	[19]
HEPS-D	4	16	2.4	0.262	-16.2	
TPS	4	18	3	0.233	-17.5	
ALBA	3.5	14	2.7	0.229	-17.5	[36]
SIRIUS	3	11	2.3	0.214	-17.9	[18]
ILSF	3.5	15	2.5	0.214	-18.0	[37]
HEPS-E	4	20	2.4	0.209	-18.1	
NSLS-II	3.5	20.5	2	0.156	-20.5	[38,39]
MAX-IV	2	11	0.6	0.095	-24.4	[40]
SKEKB	3	45	2.5*	0.052	-30.2	[41]

*Without capacitance, calculated using 2.5 pF.

3. BPM measurement accuracy and mechanical BPM pickup tolerances

The transfer impedance, which determines the strength of a useful signal, primarily affects the achievable resolution potential and is sometimes referred to as the precision of the BPM. In the user operating phase of the HEPS, when the orbit and optics corrections are complete, the BPM resolution and beam stability are of greatest importance. All random errors that change over time are important. In the preliminary beam commissioning phase of the accelerator, operators are more concerned with BPM accuracy. Before beam accumulation in the ring, the BPM measurement accuracy must satisfy the requirements of the beam-based alignment (BBA) procedure [42, 43], and the offset and roll error between the magnetic axis of the nearby quadrupole and the electric center of the BPM must be identified. An error budget of 200 μ m RMS can be distributed as follows: 1) Alignment errors of the BPM with respect to the adjacent quadrupole. 2) The electro-mechanical

offset of the BPM caused by mechanical tolerances and asymmetries among the four buttons. 3) “Electronic” offsets of the BPM caused by differences in the gain factors among the four read-out channels, including insertion losses in the signal cables. For Error 1, each BPM comprises four target ball fiducials, with alignment accuracies of 30 and 150 μm in the transverse and longitudinal directions, respectively [44]. For Error 3, the transmission difference is ± 0.5 dB before calibration, which can be improved to ± 0.1 dB, implying a position error of $\pm 25 \mu\text{m}$. Therefore, the minimization of Errors 1 and 3 is achieved by the alignment procedure [45] and pilot tone calibration technique [5]. In the BPM manufacturing stage, we mainly focused on Error 2, which depends on the mechanical tolerances of the BPM chamber, accidental and manufacturing errors and tolerances on the feedthroughs, and button location accuracy after welding. For the five types of BPMs shown in Fig. 1, Types B and C are similar to Type A. Therefore, we focused on the effects of the tolerances of only three types of BPMs on the error in the beam position measurement.

3.1 Theoretical analysis

As shown by Eq. (2), for a given operating frequency ω , the output signal of an individual button is mainly determined by the button radius r_b , the distance between the button and the center of the pipe b , and button capacitance C_b . To analyze the non-linear beam position behavior, we must begin with the normalized horizontal and vertical raw beam positions [21] because they are acquired by read-out electronics.

$$X_{\text{raw}} = \frac{V_A - V_B - V_C + V_D}{V_A + V_B + V_C + V_D}, \quad Y_{\text{raw}} = \frac{V_A + V_B - V_C - V_D}{V_A + V_B + V_C + V_D}, \quad (7)$$

where V_i ($i=A, B, C, D$) represents the voltage signal amplitude of the button i . The true position of the beam (x, y) is measured by approximating the non-linear beam position behavior $x=f(X_{\text{raw}}, Y_{\text{raw}})$ and $y=f(X_{\text{raw}}, Y_{\text{raw}})$ using a polynomial expansion,

$$X = \sum_{i=0}^n \sum_{j=0}^i A_{i-j,j} X_{\text{raw}}^{i-j} Y_{\text{raw}}^j, \quad Y = \sum_{i=0}^n \sum_{j=0}^i B_{i-j,j} X_{\text{raw}}^{i-j} Y_{\text{raw}}^j, \quad (8)$$

where A_i and B_i are the horizontal and vertical polynomial coefficients, respectively, and n is the polynomial order. A_0 and B_0 are the offsets, A_1 and B_1 are the BPM position sensitivity constants in the horizontal and vertical directions, respectively, and A_2, B_1, A_3 , and B_3 are higher-order coefficients related to the coupling between the horizontal and vertical planes. A_1 and B_2 are the most important parameters of the BPM and are typically in terms of k or S , where $k = 1/S$. This is the proportionality constant between the beam displacement and X_{raw} or Y_{raw} and is usually referred to as the position-sensitivity constant [21]. The units of k and S are mm and %/mm, respectively. A_1 is k_x and B_2 is k_y . For a circular pipe without errors, $A_0 = B_0 = 0$ and $k_x = k_y$. In the central area of the pipe, where $x-y$ coupling can be ignored, the two planes are orthogonal, and the position response is almost linear: $x = A_1 \times X_{\text{raw}} = k_x \times X_{\text{raw}}$, and $y = B_2 \times Y_{\text{raw}} = k_y \times Y_{\text{raw}}$. An oval pipe (Types D and E) was treated as circular, and $A_1 (k_x)$ and $B_2 (k_y)$ were calculated as follows [46]:

$$A_1 = B_2 = k_x = k_y = \frac{b(\alpha/2)}{\sqrt{2}\sin(\alpha/2)}, \quad (9)$$

where α is the cover angle of the button. The distances from the center of the pipe to the button b

were 11, 16, and 20 mm for the three types of BPMs, and k was 7.8, 11.3, and 14.1 mm, respectively.

By assuming that the mechanical characteristics of one of the four symmetrically arranged button electrodes deviate from the nominal value (for example, a difference in the button radius or button capacitance due to mechanical tolerances), the symmetry can be considered perturbed, which results in an undesired electro-mechanical BPM pickup offset, as summarized in Fig. 4. Figures 4a–c correspond to r_b , C_b , and b , respectively. Here, we assumed variations in only one of the button electrodes, while the other three electrodes remained unchanged at their nominal values. Based on Eqs. (2), (7), and (8), the absolute value of the electro-mechanical offset is proportional to the deviation. The slope represents the sensitivity of the electro-mechanical offset to deviation, and r_b was found to be the most sensitive parameter.

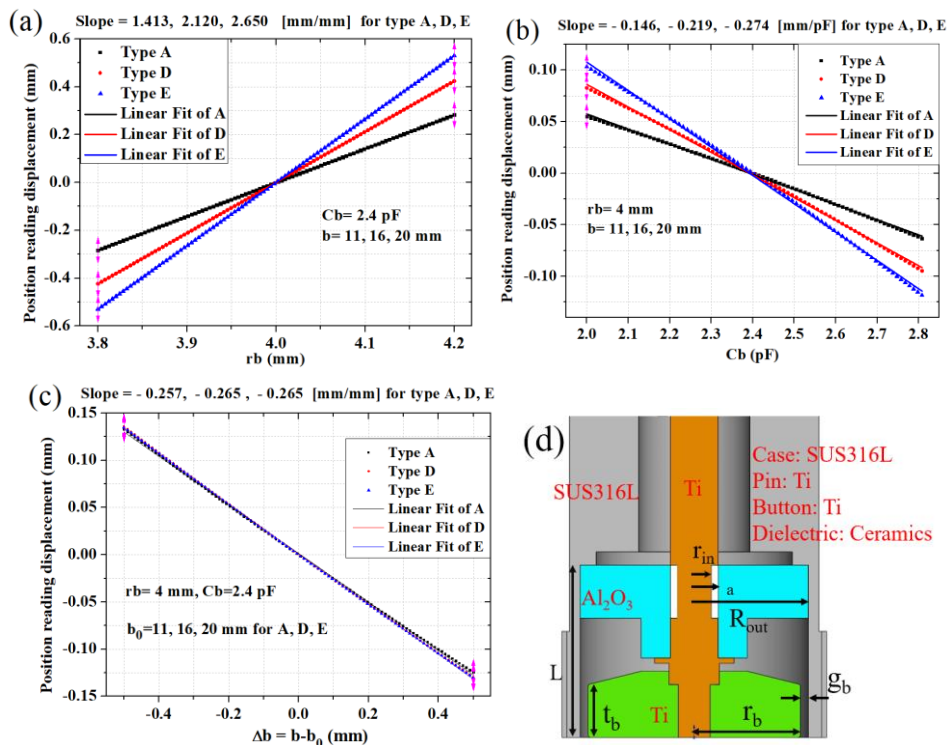


Fig. 4 (Color online) Electro-mechanical offsets of three types of BPMs, where $b = 11, 16$, and 20 mm. **(a)** $C_b = 2.4$ pF. **(b)** $r_b = 4$ mm. **(c)** $r_b = 4$ mm, and $C_b = 2.4$ pF. **(d)** Basic structure of the feedthrough with the button. The standard values are $t_b = 2$ mm, $r_b = 4$ mm, $g_b = 0.3$ mm, and $R_{out} = 4.3$ mm.

3.2 Button capacitance

Unlike the hypothetical scenario of the independent effects of the button radius r_b and capacitance C_b on the transfer impedance, we subsequently included the dependency $C_b = f(r_b)$. The capacitance of the button is mainly determined by the thickness of the button t_b , the gap between the button and pipe g_b , and the button radius r_b , as shown in Fig. 4d. Button capacitance can be inferred using time-domain reflectometry (TDR) analysis. The rise time t_{rise} of the reflected signal to an ideal step input signal, which results in reflection from button capacitance termination, allows the determination of the button capacitance [25, 27],

$$C_b = \frac{t_{\text{rise}}}{2.2Z_0}, \quad (10)$$

where $Z_0 = 50 \Omega$ is the characteristic impedance of the coaxial transmission line attached to the feedthrough. The TDR measurement results of a typical HEPS button feedthrough were $t_{\text{rise}} = 262.7 \pm 0.5$ ps and $C_b = 2.388 \pm 0.005$ pF, where the error is the standard deviation of multiple measurements of the same button. The TDR test, conducted using a Tektronix DSA8200 digital serial analyzer equipped with an 80E04 sampling module, was performed in a constant temperature and humidity environment. In addition to the experimental TDR measurements, a numerical electrostatic analysis was performed using the CST Studio Suite electrostatic solver to calculate the capacitance of the button. As shown in Fig. 5a, by disregarding the contribution of the ceramics and pin and by applying a known potential V_b to the button, the capacitance can be obtained using

$$C_b = \frac{Q}{V_b}, \quad (11)$$

where Q denotes the charge induced by the button. Figure 5b shows the capacitances numerically calculated using this electrostatic approach with CST Studio software.

In Fig. 5b, mesh densities of 10, 30, 50, and 90 correspond to the total number of mesh cells of 1×10^4 , 5×10^4 , 1×10^5 , and 5×10^5 , respectively. The minimum mesh cell sizes were 80, 14, 8, and 1 μm . By increasing the number of mesh cells, the capacitance converged to 2.36 pF, which differs by only 0.03 pF from the TDR result. The simulation results were consistent with the experimental results. Figures. 5c and d reveal that the capacitance was proportional to r_b and inversely proportional to g_b , and Fig. 5e indicates that $C_b = f(r_b)$ behaved differently with respect to the geometric parameters (in this case, $g_b = 0.3 \text{ mm}$ or $R_{\text{out}} = 4.3 \text{ mm}$). The slopes for the two cases were 0.61 and 10.65 pF/mm, which suggests that the capacitance was more sensitive to r_b than g_b , with a constant R_{out} . Moreover, $C_b = f(R_{\text{out}})$ behaved in a non-linear manner (see the red trace in Fig. 5e). Because the button and feedthrough housing are manufactured separately, it seems more realistic to maintain the mechanical tolerance of R_{out} at a reasonably low value, whereas the gap g_b depends on brazing and may suffer from greater uncertainty. The tolerances of r_b , R_{out} , and g_b were set as ± 0.015 , ± 0.015 , and ± 0.05 mm, respectively, after a discussion with the button feedthrough manufacturer, and the test results showed that most of the production satisfied our requirements.

3.3 Analysis of the mechanical tolerances of a single button electrode

Let us assume that r_b of button electrode A is larger than the radius of the other buttons of the BPM pickup. We would expect the output voltage signal $V_A > V_B = V_C = V_D$, which would result in an electromechanical BPM pickup offset owing to the broken symmetry. However, considering the effects of r_b on C_b , as r_b increases, g_b decreases and C_b increases, which consequently decreases the signal output voltage. This means that the effects of varying r_b on the button area and varying capacitance on the signal output strength partially cancel out. This is illustrated in Fig. 5f via a numerical simulation using CST Studio with varying r_b . Compared with the analytical results shown in Fig. 4, the numerical simulation correctly considered the effect $C_b = f(r_b)$. The trace $V_A = f(r_b)$ in Fig. 5f indicates a gradual increase in V_A for $r_b < 3.9 \text{ mm}$, followed by a sharp decrease for $r_b > 4.0 \text{ mm}$. In the regime $3.9 < r_b < 4.0 \text{ mm}$, the two effects canceled each other, and V_A was almost

insensitive to tolerances of r_b , in contrast with the results shown in Fig. 4a.

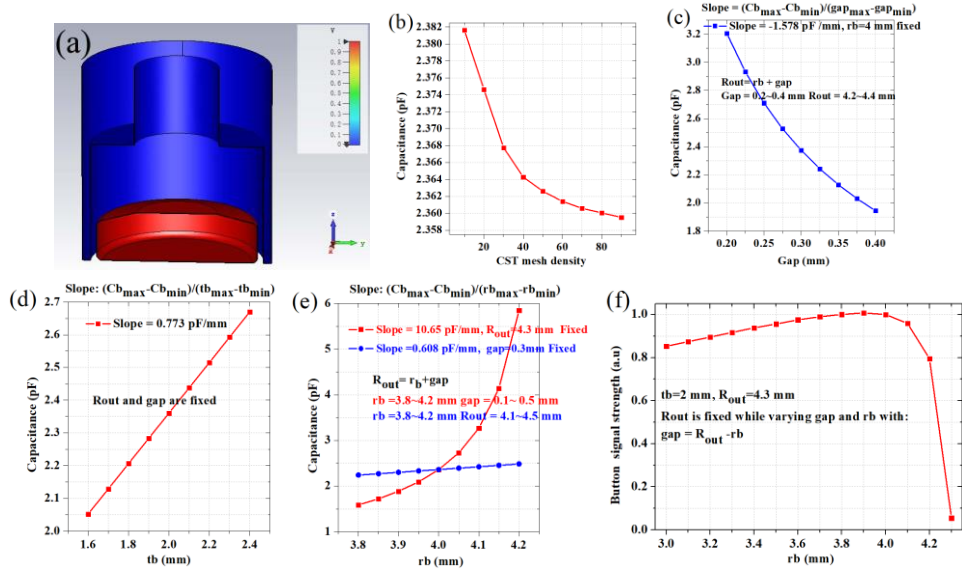


Fig. 5 (Color online) (a) C_b calculated using the static electric field solver of CST; the potential of the button was set to 1 V. (b) C_b vs. mesh densities. (c) C_b vs. g_b , $r_b = 4$ mm, $R_{out} = r_b + g_b$. (d) C_b vs. t_b . (e) C_b vs. r_b . (f) Relative signal strength vs. r_b .

During the manufacturing of the HEPS BPMs, button feedthroughs were first manufactured and sorted based on capacitance and mechanical size, as shown by the red trace of Fig. 1f (the design length between the button and the welding point was 20 mm). Subsequently, they were welded to the BPM housing body. According to the three-coordinate measuring machine (CMM) results, compared to the tolerances (0 to -0.03 mm) of the mechanical dimensions (20 mm) of the feedthrough, the welding process resulted in a larger deformation of approximately 0.05–0.1 mm, depending on the welding current. This altered, that is, retracted, the radial location of penetration in the BPM housing, resulting in an electro-mechanical offset. Assuming that welding caused a 0.3-mm misalignment only on Button A, as indicated in Fig. 6a, the entire mapping of the non-linear BPM position characteristic was altered, as indicated in the CST numerical simulation (Fig. 6a) by the shift in the blue hollow points to the red solid points. The red grid indicates the effect of the 0.3-mm button misalignment on the linear fitting of X_{raw} and Y_{raw} , where $X_{\text{raw}} = Y_{\text{raw}} = 0$ is the electrical center. The electro-mechanical offset caused by the 300- μm alignment error on the button was 380 μm in the horizontal direction and 390 μm in the vertical direction. A button is defined as positive/negative if it is retracted/protruding, as shown in Fig. 6. The values obtained by CST were significantly larger than the simplistic analytical assumptions, giving a 77- μm offset based on the slope of Fig. 4c. In reality, the tolerance of the radial button location cannot be treated as a change in b in Eq. (2). In addition to the offset, Fig. 6a also indicates a coupling between the horizontal and vertical planes owing to the 0.3-mm misalignment of Button A, which was computed to be 49.7 mrad. Although the offset would be manageable after BBA, a correction for the coupling error is difficult; in fact, it can only be reduced if it is measured and compensated for [19]. The electro-mechanical offsets of the three types of BPMs for different button misalignments are summarized in Fig. 6b. The slopes in the upper graph are larger than those in Fig. 4c. This is because Eq. (2) does not correctly consider the change in the image charge distribution for a misaligned button. Fig. 6c summarizes the effects of the x – y coupling due to button misalignment. The coupling effect was

similar for all three types of BPMs, with a slope of (170 ± 10) mrad/mm. Figure 6d shows the electro-mechanical offset for different values of r_b while R_{out} was maintained at 4.3 mm. As the limitations on the accuracy of the numerical computations, the traces in Fig. 6c and d reveal several unphysical, sporadic “jumps.” Because the analysis indicates that the BPM offset is particularly sensitive to the r_b parameter, we defined the dimensions with tolerances of $r_b = (4 \pm 0.015)$ mm.

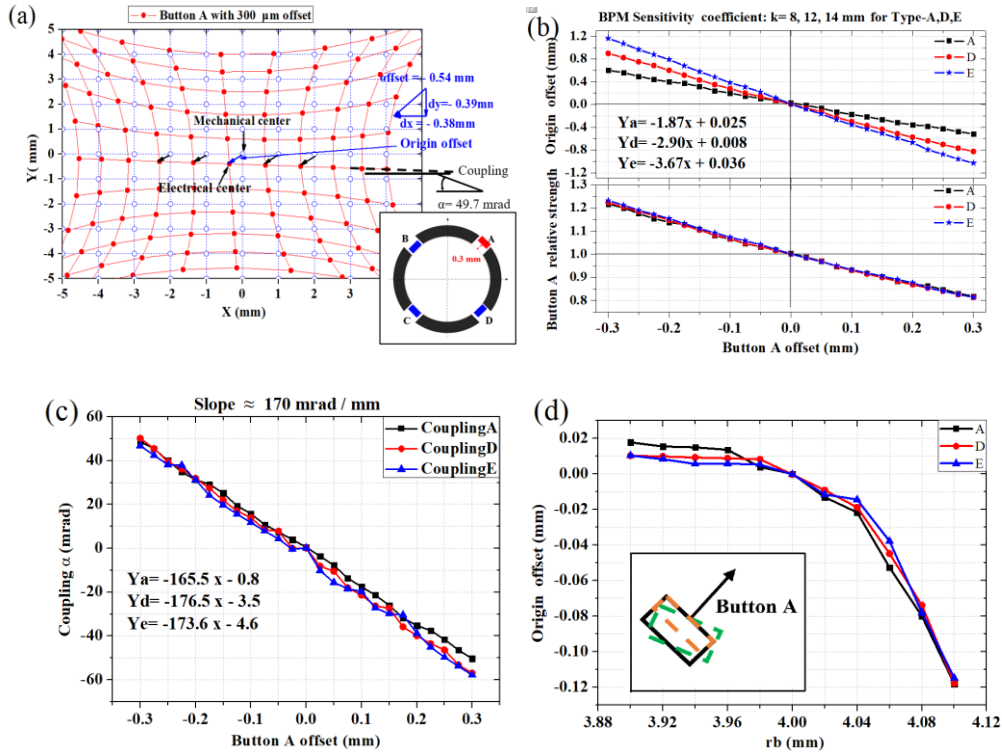


Fig. 6 (Color online) **(a)** Mapping results for Button A retracted by 0.3 mm; $x = k \times X_{\text{raw}}$, $y = k \times Y_{\text{raw}}$, $A_0 = A_2 = B_0 = B_1 = 0$, $k = A_1 = B_2 = 8$ mm. **(b)** Electro-mechanical offset and signal strength caused by button offset. $k = A_1 = B_2 = 8, 12$, and 14 mm for three types of BPMs as an approximation of 7.8, 11.3, and 14.1 mm, respectively. **(c)** Coupling caused by button offset. **(d)** Electro-mechanical offset vs. R_b .

Furthermore, we analyzed the effects of another imperfection, that is, a button roll error, in which a single button experiences unwanted rotation, as shown in the inset of Fig. 6d. The corresponding BPM errors, including the offset and coupling, were found to be significantly smaller than the button misalignment error and were difficult to resolve via numerical analysis using the CST software for a typical number of mesh cells (1×10^6 – 10×10^6).

3.4 Summary of the effects of various mechanical button tolerances and misalignments

To evaluate the accuracy of the CST numerical calculations, A_i and B_i in Eq. (8) were determined using least squares to fit X_{raw} and Y_{raw} . The fitting error $\sqrt{(x-x_{\text{fit}})^2 + (y-y_{\text{fit}})^2}$ was then calculated, where (x, y) and $(x_{\text{fit}}, y_{\text{fit}})$ are the true beam position used as the input for the CST numerical analysis and the fitted position value from the polynomial approximation given by Eq. (8). A contour plot of the error for the $5 \text{ mm} \times 5 \text{ mm}$ region is shown in Fig. 7. Figure 7a shows the results for the Type-A BPM with ideal dimensions and zero tolerances, where A_0, B_0, A_2 , and B_1 should theoretically be

0. The linear fit coefficients based on the CST simulations were $A_0 = -0.0146$, $B_0 = -0.0021$, $A_2 = 7.19 \times 10^{-4}$, and $B_1 = 4.61 \times 10^{-4}$, which reflects the accuracy of the calculation limited by the numerical accuracy of the CST analysis. Fig. 7b shows the effect of a 0.3-mm misalignment of Button A, Fig. 7c shows the effect when Button A was rotated by 100 mrad (5.7°), and Fig. 7d shows the effect of a 0.1-mm deviation of the button radius. These misalignments and tolerances resulted in offset and coupling errors, as indicated by the A_i and B_i coefficients of the linear fit. Button misalignment was the most significant error source for both the electro-mechanical offset and the x - y coupling; however, it did not affect the position sensitivity constant (k_x , k_y) and reduced the linear measurement region (blue area in Fig. 7, where the error is smaller than 0.2 mm). In contrast, the roll error of a single button was insensitive to the BPM offset and coupling but exhibited an error in the sensitivity constant k of the BPM. k_x (A_1) in Fig. 7c increased and k_y (B_2) decreased compared with those in Fig. 7a. Finally, the tolerance error in the button radius did not seem to significantly affect any of these three parameters. The fit coefficient results for $r_b = 4.1$ mm, as shown in Fig. 7d, did not differ significantly from those of an ideal BPM. When r_b was 3.9 mm ($R_{out} = 4.30$ mm), the difference was even less significant. These effects are summarized in Table 2.

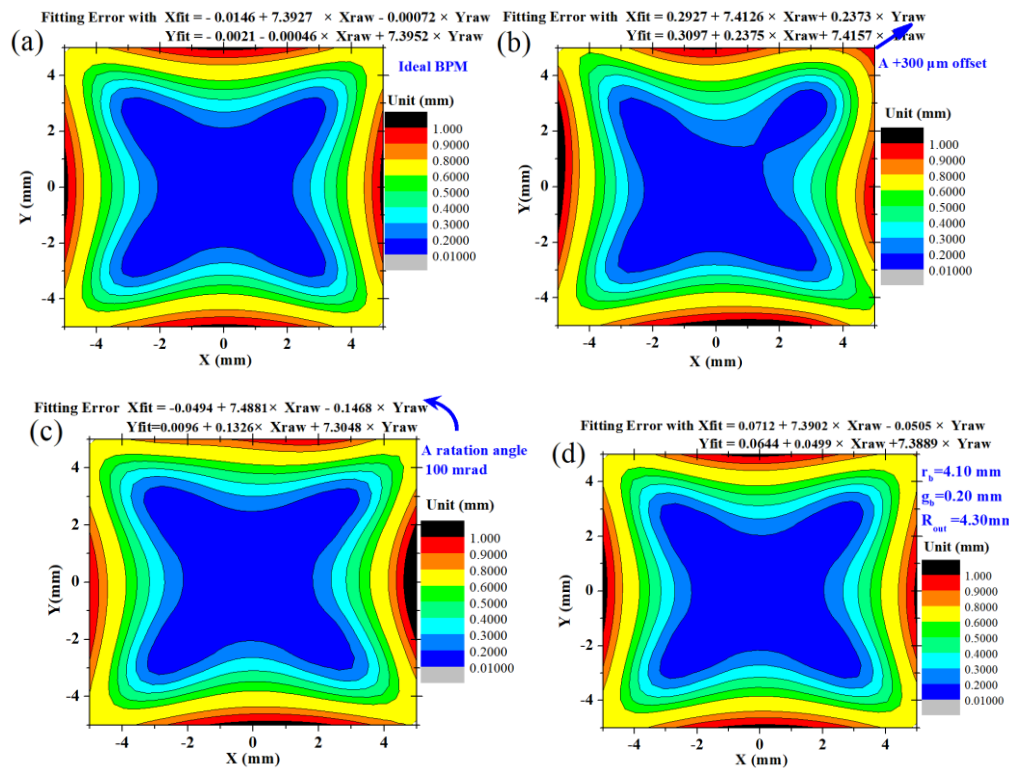


Fig. 7 (Color online) Fitting error; A_0 (offset), A_1 (position sensitivity coefficient) and A_2 (x - y coupling coefficient). **(a)** Ideal BPM. **(b)** Button A with a 300- μ m offset. **(c)** Button A with a 100-mrad angle error; the location azimuthal angle θ was 50.7° instead of 45°. **(d)** Radius and gap of Button A were 4.1 and 0.2 mm, respectively.

Table 2 Fitting results of mapping; the unit of b and r_b is mm, and the unit of θ (the azimuthal angle of Button A) is degrees

	Electro-mechanical offset A_0/B_0	Sensitivity constant $k_x(A_1)/k_y(B_2)$	Coupling A_2/B_1
Standard $b=11$, $r_b=4$, $\theta=45$	-0.014/-0.002	7.392/7.395	0.000/0.000
$b=11.3$, $r_b=4$, $\theta=45$	0.293/0.310	7.421/7.415	0.237/0.237
$b=11$, $r_b=4$, $\theta=50.7$	-0.049/0.009	7.488/7.305	-0.147/0.133
$b=11$, $r_b=4.1$, $\theta=45$	0.071/0.064	7.390/7.389	-0.051/-0.050
b	Sensitive	Insensitive	Sensitive
θ	Insensitive	Sensitive	Insensitive
r_b	Insensitive	Insensitive	Insensitive

A_i , B_i , and the fitting errors depend on parameters such as the fitting order n , scan range, and step [47–49]. The distribution of the fitting error $\sqrt{(x-x_{\text{fit}})^2 + (y-y_{\text{fit}})^2}$ for a real BPM (Type A), where X_{raw} and Y_{raw} were recorded by a stretched wire calibration system with a scan range of $6 \text{ mm} \times 6 \text{ mm}$ and a step of 0.25 mm , is shown in Fig. 8a. The average values of $\sqrt{(x-x_{\text{fit}})^2}$ and $\sqrt{(y-y_{\text{fit}})^2}$ were 0.5080 and 0.4874 for a linear fit, and 0.4950, 0.4862, 0.1164, 0.0971, 0.1113, 0.0964, 0.0454, 0.0387, 0.0410, and 0.0363 mm for $n = 2$ –6. Figures 8b and c show the average values of the fitting error and sensitivity constant k for different scan ranges. Finally, two groups of fitting coefficients with $n = 5$ were used for position measurement: a group of coefficients based on a calibration range of $x = y = 4 \text{ mm}$ for the user's normal operation phase and that with $x = y = 7 \text{ mm}$ for the preliminary commissioning phase.

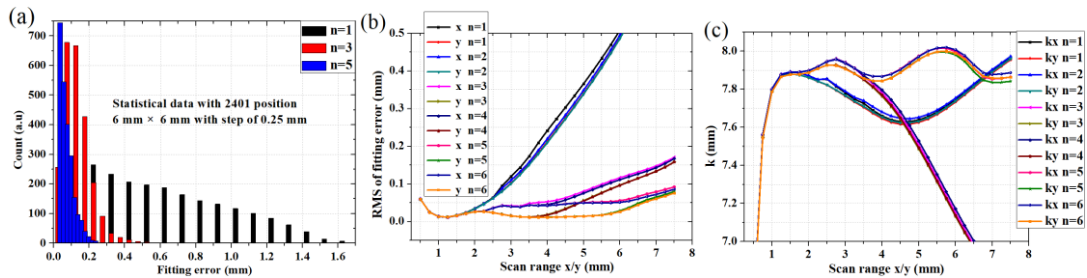


Fig. 8(Color online) (a) Fitting error distribution $\sqrt{(x-x_{\text{fit}})^2 + (y-y_{\text{fit}})^2}$ for a scan range of $6 \text{ mm} \times 6 \text{ mm}$ with a step of 0.25 mm . (b) Average value of the error and (c) k for different scan ranges with a step of 0.25 mm .

3.5 Measurement of the HEPS button BPMs

Figure 9 summarizes the most relevant mechanical and electrical measurements taken on 69 fully assembled Type-D BPMs (booster BPMs) utilizing 276 button feedthroughs (Figs. 9a and b) and 500 individual button feedthroughs (Figs. 9c and d). Figure 9a summarizes the statistics of the CMM measurements on the BPM vacuum chamber radius b , which had a nominal value of 16.096 mm . Figure 9b shows the difference between the minimum and maximum values of b measured at the location of the four buttons in the BPM unit, which relates to the discussion on button misalignment

(see previous paragraph). Figures 9c and d show the C_b results measured using the TDR method and the measurement of r_b using an optical microscope with a maximum magnification of 200. Fig. 9e shows an example of the optical microscope result of R_{out} . The RMS values of b and Δb ($b_{max} - b_{min}$) for the BPM pickups and C_b and r_b for the button feedthroughs were 31, 22 μm , 0.042 pF, and 6.6 μm , respectively. During manufacturing of the BPMs, feedthroughs were selected based on the sorting of C_b before welding. The difference between the maximum and minimum C_b in a BPM did not exceed 0.02 pF, and the effect of the difference in capacitance on the position measurement was negligible.

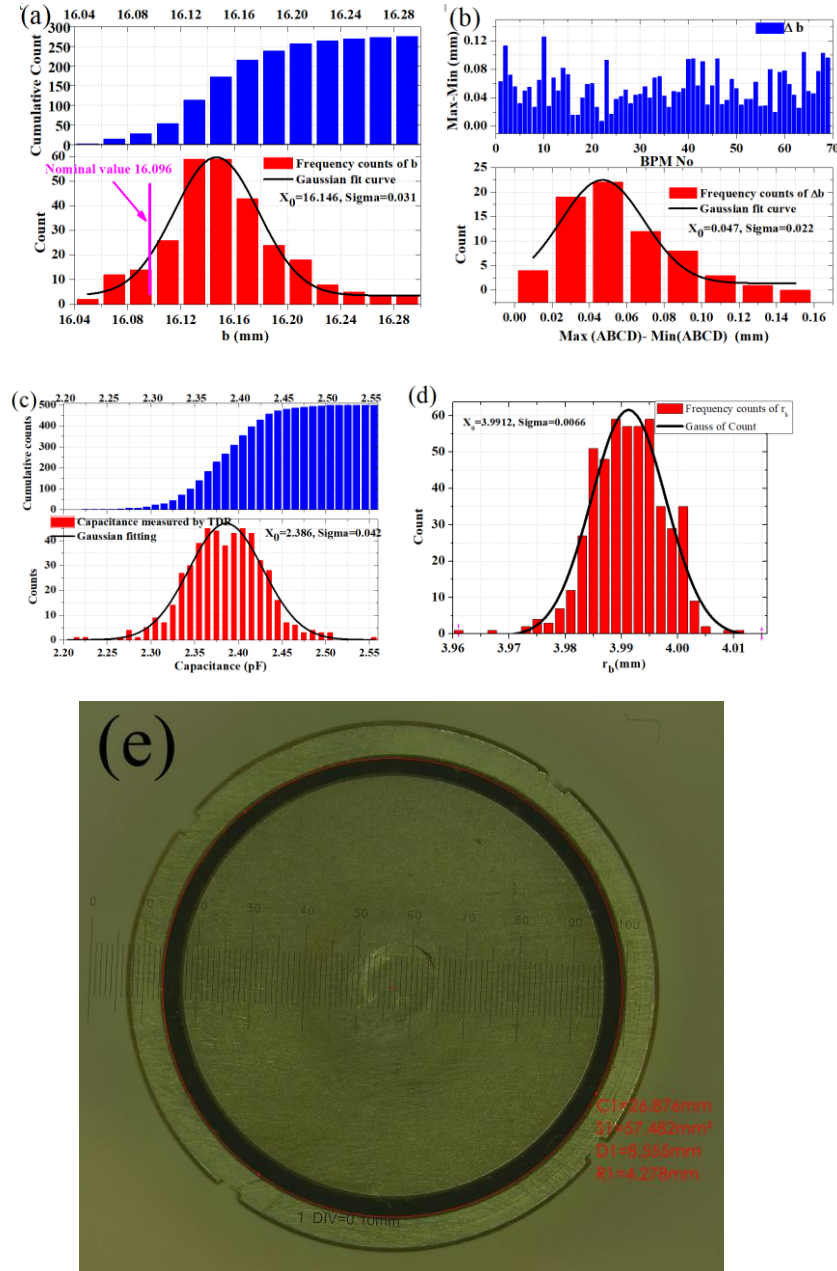


Fig. 9 (Color online) (a) Statistics histogram showing the distance from the button to the center of the BPM pipe. Sixty-nine booster BPMs (Type D) were measured using the CMM. (b) Statistics histogram of the deviation of b for four buttons in a BPM. (c), (d) C_b and r_b measurement results for 500 feedthroughs, respectively. (e) Optical microscope result of R_{out} (R_1), diameter D_1 , area S_1 , and circumference C_1 .

4. Analysis of trapped resonance modes

In addition to the transfer impedance, the beam coupling impedance due to wake fields is an important parameter in the BPM design process. The analytical expression for the longitudinal beam coupling impedance of a button-style BPM electrode given in Eq. (3) underestimates the impedance value because it is based on EM fields that contribute to the output signal. Unfortunately, the button-style BPM has eigenmodes that couple to the beam field and occur as “trapped” modes, which do not dissipate their power during external termination. These have been investigated using different methods [37, 41, 50].

The beam coupling or wake impedance is the Fourier transform of the time-domain wake potential, which can be analyzed by a numerical simulation. In this study, this was performed using the CST software suite. Figures 10a and b show the BPM model of the CST calculation and the longitudinal wake impedance for different dielectric constants of the insulator used in the button feedthrough. Six eigenmodes were excited in the frequency range 10–25 GHz, but no mode was present below 10 GHz. The frequencies of the six modes are presented in Table 3. The analytical frequencies listed in Table 3 are expressed as follows [18]:

$$f^{\text{Hm1p}} = \frac{1}{\sqrt{\epsilon_r} 2\pi} \sqrt{\left(\frac{2m}{R_{\text{in}} + R_{\text{out}}}\right)^2 + \left(\frac{p\pi}{l_{\text{coax}}}\right)^2}, \quad (12)$$

where l_{coax} is the longitudinal length of the coaxial structure, and ϵ_r is the relative permittivity of the material between the inner and outer conductors. From the theory of circular waveguides, we can compare the analytically expected mode frequencies with those of the numerical analysis.

As shown in Fig. 4d, several sections of the coaxial insulation part of the feedthrough were inhomogeneous and consisted of two materials with different permittivities: ceramics ($\epsilon_r = 9.9$) and vacuum or air ($\epsilon_r = 1$). For these sections, we calculated the effective dielectric constant ϵ_e based on the relative volumes and permittivities of the two dielectric materials and applied this result instead of ϵ_r to Eq. (12). The mechanical parameters and results are listed in Table 4, where only the thicker homogeneous part of the ceramic insulator (upper part of Fig. 4d) was evaluated. As predicted by Eq. (12), the higher the relative permittivity, the lower the frequency of the trapped modes. As indicated by the red arrows in Fig. 10b, if the relative permittivity of the ceramic $\epsilon_{\text{ceramic}}$ increased, the frequencies of the second, third, and fourth modes shifted to lower values, which implies that these modes were trapped in the ceramic sections, whereas the frequencies of the other three modes (that is, the first, fourth, and fifth modes) barely changed. This implies that they were trapped, for example, by the gap between the button and housing. The mesh grid of the CST calculation barely changed during the permittivity scan.

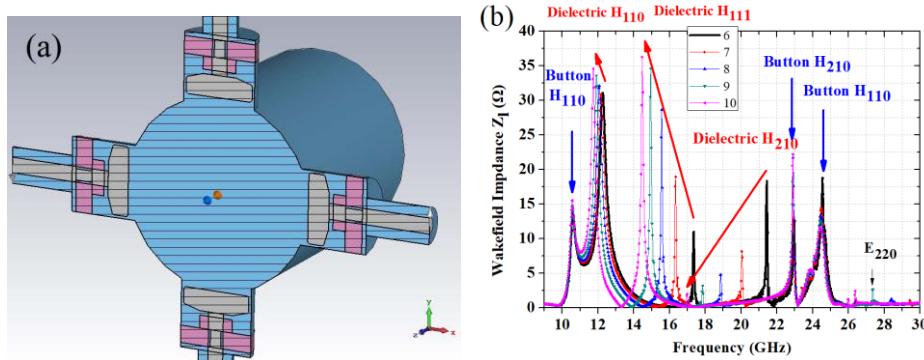


Fig. 10 (Color online) (a) CST simulation model. (b) Wake field impedance of the HEPS BPM

with the relative permittivity of the ceramics adjusted from 6 to 10; a bunch length of 10 ps (RMS) was assumed.

Table 3 Trapped mode frequencies for the HEPS BPM calculated using CST

	Frequency (CST)	Frequency (Analytical)	Mode
	(GHz)	(GHz)	
1	10.44	11.51	Button H_{110}
2	11.74	9.74	Ceramics H_{110}
3	14.47	14.57	Ceramics H_{111}
4	17.00	19.48	Ceramics H_{210}
5	22.90	23.01	Button H_{210}
6	24.16	24.32	Button H_{111}

Table 4 Trapped mode frequencies for the HEPS BPM calculated using Eq. (12)

r_{in} (mm)	R_{out} (mm)	a (mm)	l_{coax} (mm)	ϵ_r /	ϵ_e /	H_{110} (GHz)	H_{210} (GHz)	H_{111} (GHz)	H_{211} (GHz)
0.65	4.3	0.9	7	9.9	3.92	9.74	19.48	14.57	22.30
4	4.3	/	7	1	1	11.51	23.01	24.32	31.45

Figure 11 shows the distribution of the surface current for the button H_{110} mode (a) and ceramic insulator H_{110} mode (b). The surface current and energy were primarily concentrated in the associated structure. Because the gap between the button and the distance to the ceramic insulator was small, some energy remained in the button gap area, even for the ceramic-related mode, as shown in Fig. 11b.

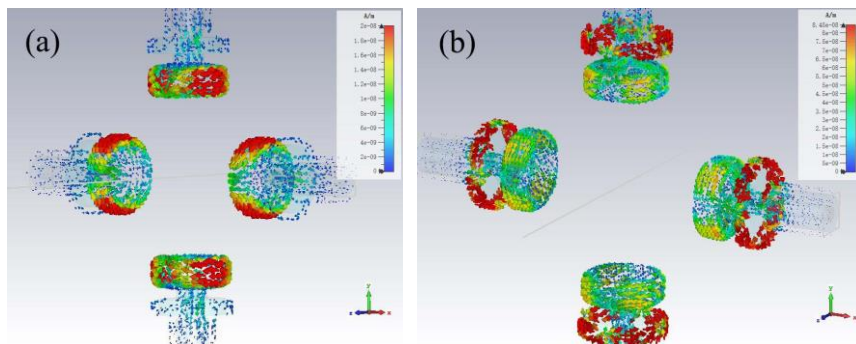


Fig. 11 (Color online) (a) Surface current distribution for the button-related mode H_{110} , where $f=10.44$ GHz, and the (b) ceramics-related mode H_{210} , where $f=17.00$ GHz.

The analysis and visualization of the EM field of a trapped mode in the cross-sectional area was difficult because the gap g_b was small. Therefore, we analyzed the EM field in the cross-section of the ceramic area. Figure 12 shows the electric field distributions at 11.74 GHz (H_{110}) and 17.00 GHz (H_{210}) for the cross-section in the ceramic area, which clearly identifies the H_{11} dipole and H_{21} quadrupole mode pattern. Figure 13 shows the electric field at 11.74 GHz (H_{110}) and 14.47 GHz (H_{111}) in the longitudinal section view along the signal propagation direction, with H_{110} in phase and

H_{111} out of phase. All six trapped mode frequencies are listed in Table 3, and all are transverse electric (TE) modes. The transverse magnetic mode exhibited a higher frequency and a significantly lower field strength than the TE mode, as shown in Fig. 10b. Figure 13c shows the electric field distribution of the transverse magnetic E_{220} mode in the cross-section of the ceramic area, which had an eigenfrequency of 27.34 GHz. However, this will have only a minimal impact on a beam with a high frequency and low shunt impedance.

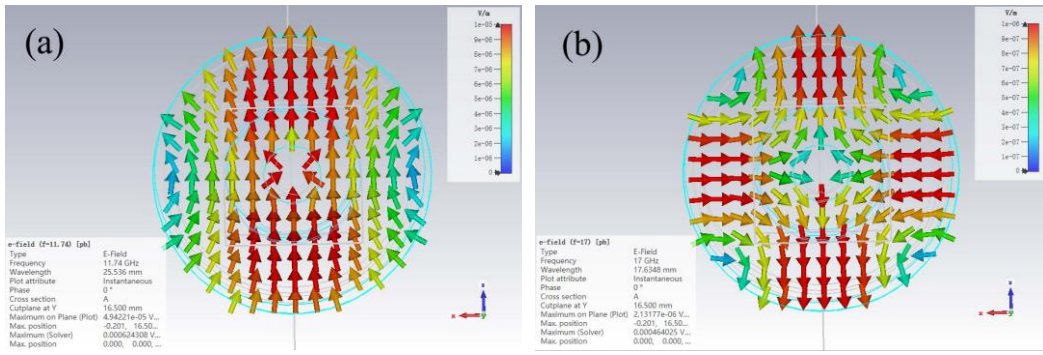


Fig. 12 (Color online) Electrical field distribution of ceramics. (a) H_{110} , (b) H_{210} .

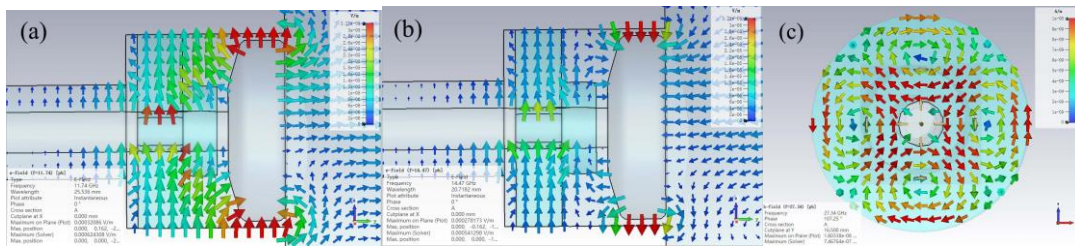


Fig. 13 (Color online) Electrical field distribution of ceramics. (a) H_{110} . (b) H_{111} . (c) E_{220} .

5. Thermal analysis

The real component of the longitudinal beam coupling impedance corresponds to the energy loss of the beam, and the imaginary component corresponds to the energy exchange between the beam and button capacitance, which may induce beam instability and breakup effects. The loss factor k_{loss} for an RMS bunch length of 3 and 6 mm was 15.2 and 2.43 mV/pC, respectively, at a 200-mA current. Meanwhile, the total power loss of the four buttons was 4.06 and 0.64 W, respectively. The temperature distribution of the BPM was calculated using ANSYS software [51]. The ambient temperature was set to 25 °C, and the results are shown in Fig. 14a. The following materials were selected: stainless steel (thermal conductivity $\sigma_t = 15.1 \text{ WK}^{-1}\text{m}^{-1}$) for the BPM body, and titanium ($\sigma_t = 21.9 \text{ WK}^{-1}\text{m}^{-1}$) for the pin and button. The maximum temperature obtained on the button surface was 56 °C when a thermal power of 1 W was applied to each button. The simulation showed that materials with better thermal conductivity, such as molybdenum, can significantly reduce the increase in temperature. Thermal deformation of the button and body can cause a drift in the BPM offset, which deteriorates the long-term stability of the BPM system. The deformation results are shown in Fig. 14b, where the deformation of the support brackets at the wings was set to zero. The deformations of the pin and button were approximately 3.2 and 2.5 μm , respectively.

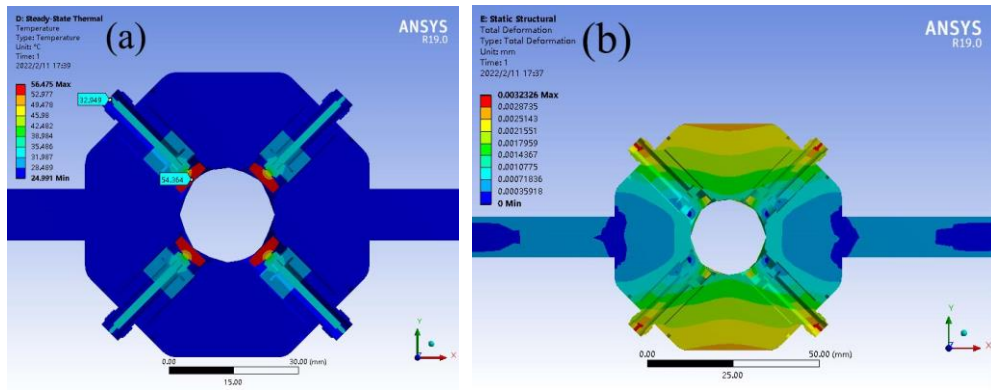


Fig. 14 (Color online) (a) Thermal analysis of the HEPS BPM (Type A). Temperature profile of the titanium button and ceramics. (b) Mechanical deformation of the BPM induced by wake field impedance.

6. Conclusion

The BPM system is one of the most important beam instrumentation and diagnostic systems for the HEPS. To achieve the required sub-micrometer orbital stability, the resolution potential and accuracy of the BPM pickups were analyzed. The BPM pickups designed for the HEPS have a reasonably high transfer impedance at the frequency of interest and provide sufficient signal power levels to the read-out electronics. The store ring (Types A, B, and C) and booster (Types D and E) BPMs have a transfer impedance of 0.38, 0.41, 0.41, 0.19, and 0.17 Ω at the 500 MHz operating frequency, respectively, according to numerical simulation. The impact of various manufacturing and assembly tolerances on the error of BPM measurement was investigated in detail. The sensitivities of the BPM measurement and the resulting measurement error to mechanical tolerances were obtained. A coupling of 49.7 mrad with 0.54 mm offsets were caused by a 0.3-mm contraction of a button. Reasonable manufacturing tolerances can be inferred from the total BPM error budget. The actual performances of the feedthroughs and BPMs were measured using different methods, and data pertaining to the button radius, button capacitance, and button positioning accuracy after welding were analyzed. The button capacitance C_b was found to be 2.4 pF, measured using TDR. The wake field impedance and trapped modes of the BPMs were analyzed based on the numerical simulation results obtained using CST software. The first trapped mode appeared to be of the H_{110} type, with a frequency of approximately 10.4 GHz. Finally, heating caused by the wake fields was analyzed, and the total power loss for the four buttons was found to be 4.06 W at a bunch length of 3 mm. ANSYS simulation results showed that a material with a higher thermal conductivity could reduce the increase in temperature.

Acknowledgments

The authors thank Dr. Ren-Xian Yuan at the Shanghai Advanced Research Institute for their help in the development of the feedthroughs. The authors thank Dr. Zhe Duan, Sai-Ke Tian, and Ou-Zheng Xiao for their helpful discussions and Xu-Jian Wang for help with BPM manufacturing.

References

[1] Y. Jiao, P. He, J. Y. Li et al., Modification and optimization of the storage ring lattice of the High Energy Photon Source. *Radiat Detect. Technol. Methods.* **4**, 415–424 (2020). <https://doi.org/10.1007/s41605-020-00189-7>

- [2] Y. Jiao, G. Xu, X.H. Cui et al., The HEPS project. *J. Synchrotron Radiat.* **25**, 1611–1618 (2018). <https://doi.org/10.1107/S1600577518012110>
- [3] Q. Qin, J. S. Cao, F. S. Chen et al., Progress of HEPS accelerator system design. in Proceedings of IPAC2019, Melbourne, Australia, 633-635 (2019). doi:10.18429/JACoW-IPAC2019-MOPRB027
- [4] J. He, Y. F. Sui, J. S. Cao et al., Preliminary study on detection and cleaning of parasitic bunches. *Nucl. Sci. Tech.* **32**, 114 (2021). doi.org/10.1007/s41365-021-00948-1
- [5] S. J. Wei, Q. Ye, Y. Y. Du et al., Brief Introduction to HEPS BPM Electronics Development, in Proceedings of IBIC2020, Brazil, (2020).
- [6] J. He, Y. F. Sui, Y. Li, et al., Beam position monitor design for the High Energy Photon Source. *Meas. Sci. Technol.* **33**, 115106 (2022). <https://doi.org/10.1088/1361-6501/ac8277>
- [7] Y. Li, J. He, Y. F. Sui, et al., Development of BPM feedthroughs for the High Energy Photon Source. *Radiat Detect. Technol. Methods.* **6**, 460-469 (2022). <https://doi.org/10.1007/s41605-022-00345-1>
- [8] X. Y. Huang, Y. Y. Wei, Y. Jiao, Preliminary investigation of the noises and updates on physics studies of FOFB in HEPS. in Proceedings of IPAC2021, Campinas, SP, Brazil, 2197-2199 (2021). doi:10.18429/JACoW-IPAC2021-TUPAB304
- [9] <https://www.aps.anl.gov/BES-Light-Sources-Beam-Stability-Workshop>, 2018 BES Light Sources Stability Workshop (2018).
- [10] Y. K. Tian, K. Ha, L. Yu et al., NSLS-II fast orbit feedback system. in Proceedings of ICALEPCS2015, Melbourne, Australia, 34-37 (2015).
- [11] X. Z. Liu, S. Q. Tian, X. Wu et al. Feedforward compensation of the insertion devices effects in the SSRF storage ring. *Nucl. Sci. Tech.* **33**, 70 (2022). <https://doi.org/10.1007/s41365-022-01052-8>
- [12] Z. Z. Wang, J. He, Z. H. Wang et al., Study on supports system of BPMs for HEPS, in Proceedings of IPAC 2017, Copenhagen, Denmark, 322-324 (2017).
- [13] <https://indico.cern.ch/event/680538>, Mechanical Engineering Design of Synchrotron Radiation Equipment and Instrumentation (MEDSI) conference.
- [14] C. Spataro, F. Lincoln, S. Shara, NSLS-II site vibration studies to characterize beamline stability (2018). doi:10.18429/JACoW-MEDSI2018-WEPH29
- [15] M. C. Rocha, A. L. Mesa, A. R. D. Rodrigues et al., High rigidity girder system for the SIRIUS machine (2018). doi:10.18429/JACoW-MEDSI2018-WEPH26
- [16] A. F. D. Morgan, Technical review of beam position button design and manufacture. in Proceedings of IBIC 2019, Malmo, Sweden, 448-452 (2019). doi:10.18429/JACoW-IBIC2019-WEAO01
- [17] M. Tobiayama, BPM electrode and high-power feedthrough – special topics wideband feedthrough, in Proceedings of IBIC2012, Tsukuba, Japan, 297-301 (2012).
- [18] H. O. C. Duarte, L. Sanfelici, S. R. Marques, Design and impedance optimization of the SIRIUS BPM button. in Proceedings of IBIC2013, Oxford, UK, 365-368 (2013).
- [19] K. Scheidt, Experience with UHV-leaks on 1500 units of BPM-buttons at the ESRF. BPM button workshop, May2-3, Dicot, UK, (2019).
- [20] P. Forck, Lecture notes on beam instrumentation and diagnostics. Joint University Accelerator School, January – March (2016).
- [21] P. Forck, P. Kowina, D. Liakin, Beam position monitors. CERN Accelerator School, Beam Diagnostics Dourdan, France, 28 May – 6 June, 187-228 (2008).
- [22] M. Wendt, BPM Systems. Proceedings of the 2018 course on Beam Instrumentation for Particle Accelerators Tuusula, Finland, 2–15 June, 373-411 (2018).
- [23] CST Studio Suite®, Version 2017, CST AG, Darmstadt, Germany (2017).
- [24] M. Kumar, L. K. Babbar, R. K. Deo et al., Modified coaxial wire method for measurement of transfer impedance of beam position monitors. *Phys. Rev. ST Accel. Beams* **21**, 052801 (2018). doi: 10.1103/PhysRevAccelBeams.21.052801
- [25] F. Marcellini, M. Serio, A. Stella et al, DAΦNE broad-band button electrodes. *Nucl. Instrum. Methods Phys. Res. A* **402**, 27-35 (1998). [https://doi.org/10.1016/S0168-9002\(97\)01083-8](https://doi.org/10.1016/S0168-9002(97)01083-8)
- [26] X. Sun, R. M. Lill, The RF bpm pickup electrodes development for the APS-MBA upgrade. in Proceedings of NAPAC2019, Lansing, MI, USA, 256-258 (2019). doi:10.18429/JACoW-NAPAC2019-MOPLO12
- [27] G. B. Zhao, R.X. Yuan, Y.B. Leng et al., Development of button-type pickup for SSRF ring. *Nucl. Sci. Tech.* **25**, 060103 (2014). doi: 10.13538/j.1001-8042/nst.25.060103
- [28] R. E. Shafer, Beam position monitoring. *AIP Conference Proceedings* **249**, 601, 627-631 (1992). doi: 10.1063/1.41980
- [29] H. Schmickler, Beam position measurement system design. in Proceedings of IBIC2015, Melbourne, Australia, 618-624 (2015).

- [30] M. Wendt, Direct (under) sampling vs. Analog down conversion for bpm electronics. in Proceedings of IBIC2014, Monterey, USA, 486-494 (2014).
- [31] P. Cameron, O. Singh, Comparative study of button BPM trapped mode heating. in Proceedings of PAC2009, Vancouver, Canada, 3392-3394 (2009).
- [32] J. He, Y. F. Sui, Y. H. Lu et al., A high sensitivity tune measurement system for BEPCII. *Radiat Detect. Technol. Methods*. **6**, 88–96 (2022). <https://doi.org/10.1007/s41605-021-00300-6>
- [33] Z. C. Chen, Y. B. Leng, R. X. Yuan et al., Beam position monitor design for a third-generation light source. *Phys. Rev. ST Accel. Beams* **17**, 112801 (2014). doi:10.1103/PhysRevSTAB.17.112801
- [34] M. J. Dufau, D. M. Dykes, R. J. Smith, Electron beam position monitor (EBPM) diagnostics for DIAMOND. in Proceedings of IPAC1999, 2096-2098 (1999).
- [35] H. Maesaka, H. Dewa, T. Fujita et al., Development and performance test of the BPM system for the SPring-8 upgrade. in Proceedings of IPAC2017, 265-267 (2017).
- [36] A. Olmos, T. Gunzel, F. Perez, BPM design for the ALBA synchrotron. in Proceedings of EPAC2006, Edinburgh, Scotland, 1190-1192 (2006).
- [37] M. Shafiee, S. A. H. Feghhi, J. Rahighi, Numerical analysis of the beam position monitor pickup for the Iranian light source facility. *Nucl. Instrum. Methods Phys. Res. A* **847**, 162–170 (2017). <https://doi.org/10.1016/j.nima.2016.11.065>
- [38] S. Dierker, NSLS-II preliminary design report, (2007).
- [39] A. Blednykh, B. Bacha, G. Bassi et al., NSLS-II storage ring bpm button development. in Proceedings of IPAC2015, Richmond, VA, USA, 748-750 (2015). doi:10.18429/JACoW-IPAC2015-MOPMN021
- [40] MAX IV Detailed Design Report, Chapter 2.9 (2010).
- [41] M. Tobiyama, H. Fukuma, K. Shibata et al., Development of button electrodes for super-KEKB rings, in Proceedings of BIW2010, 223-227 (2010).
- [42] A. Madur, P. Brunelle, A. Nadji, L.S. Nadolski, Beam based alignment for the storage ring multipoles of synchrotron SOLEIL. in Proceedings of EPAC2006, Edinburgh, Scotland, 1939-1941 (2006).
- [43] X. B. Huang, Beam-based correction and optimization for accelerators, CRC Press Taylor & Francis Group (2020). ISBN-10: 1138353167 doi: 10.1201/9780429434358
- [44] D. H. Ji, Z. Duan, Y. Jiao et al., Beam performance simulation with error effects and correction on HEPS design. in Proceedings of IPAC2018, Vancouver, BC, Canada, 4186-4188 (2018). doi:10.18429/JACoW-IPAC2018-THPMF054
- [45] C. H. Li, H. J. Wang, N. C. Zhou et al., Design and progress of mechanical support in HEPS. in Proceedings of IPAC2019, Melbourne, Australia, 4180-4182 (2019). doi:10.18429/JACoW-IPAC2019-THPTS034
- [46] G. Kube, Sensitivity estimation for the PETRA-III beam position monitors based on a boundary element method (2007).
- [47] K. Shinoe, N. Nakamura, T. Katsura et al., Design and calibration of pickup-electrodes for beam position monitoring at SOR-RING. in Proceedings of PAC1993, 2337-2339 (1993).
- [48] K. Satoh, M. Tejima, Calibration of KEKB beam position monitors. in Proceedings of PAC1997, 2087-2089 (1997). doi: 10.1109/PAC.1997.751116
- [49] S. Hiramatsu, Beam position monitors for circular accelerators. in Proceedings of IBIC2012, Tsukuba, Japan, 590-601 (2012).
- [50] M. Makaki, H. Dewa, T. Fujita et al., Design optimization of button-type bpm electrode for the SPring-8 upgrade. in Proceedings of IBIC2016, Barcelona, Spain, 360-363 (2016).
- [51] <http://ansys.com> for ANSYS®, ANSYS, Inc